Mechanical Properties and Dislocation Structure Evolution in Ti6Al7Nb Alloy Processed by High Pressure Torsion

MILOŠ JANEČEK, JOSEF STRÁSKÝ, JAKUB ČÍŽEK, PETR HARCUBA, KRISTÍNA VÁCLAVOVÁ, VERONIKA V. POLYAKOVA, and IRINA P. SEMENOVA

Ultrafine-grained biocompatible Ti-6Al-7Nb alloy was produced by high pressure torsion (HPT). Lattice defects—vacancies and dislocations—investigated by positron annihilation spectroscopy, observations by scanning electron microscopy, and microhardness evaluation are linked to the strain imposed by different numbers of HPT revolutions and to the distance from the specimen center. Positron annihilation spectroscopy showed significant increase of dislocation density and concentration of vacancy clusters after ½ of the HPT revolution. Microhardness increases by 20 pct with increasing strain, but it is heterogenous due to duplex microstructure. The heterogeneity of the microhardness increases with increasing strain, suggesting that a heavily deformed and fragmented $\alpha + \beta$ lamellar microstructure is more hardened than primary alpha grains. The defect structure is homogenous after ½ HPT revolution, while the microhardness becomes homogenous after 3 HPT revolutions only.

DOI: 10.1007/s11661-013-1763-2

I. INTRODUCTION

FOR several decades, titanium alloys have been the most used material for load-bearing orthopedic implants.[1] Their unique combination of properties includes extreme corrosion resistance, relatively high strength, sufficient biocompatibility, and moderate elastic modulus.[2] Commercially pure titanium is used in some dental and orthopedic applications mainly due to its excellent biocompatibility. However, limited strength (up to 500 MPa) disallows using commercially pure titanium as a material for orthopedic endoprostheses, which constitute a majority of the market of metallic implants. The most commonly used one is still one of the oldest Ti alloys—Ti-6Al-4V—that belongs to the alpha + beta alloys. Despite the generally good properties of this alloy, there are several limitations. A special concern relates to the presence of vanadium which is considered to be a toxic element. A similar alpha + beta Ti alloy Ti-6Al-7Nb has been developed to avoid the adverse effect of vanadium.[3,4] Ti-6Al-7Nb alloy has similar mechanical properties and undergoes a similar phase transformation as the common Ti-6Al-4V alloy.

The mechanical and other essential properties determining the application of titanium alloys may be improved by refining the grain size to the submicrometer or even nanometer level. A variety of special techniques are used for the production of bulk ultrafine-grained (UFG) materials, *e.g.*, equal channel angular pressing (ECAP),[5] high pressure torsion (HPT),[6,7] accumulative roll bonding (ARB),[8] twist extrusion,[9] or multidirectional forging.[10] Among these techniques, which introduce severe plastic deformation (SPD) in the material, HPT provides an opportunity for achieving exceptional grain refinement often to the nanometer level in many FCC and HCP metals and alloys.[11] Due to the fundamentally non-homogenous deformation by HPT, important properties evolve with the number of HPT revolutions and with the distance from the specimen center. HPT therefore allows getting fundamental knowledge of the evolution of the structure refinement and the nature of physical strengthening.

The aim of this study is therefore twofold:

(a) to fabricate the ultrafine-grained structure in the Ti-6Al-7Nb alloy by HPT and
(b) to characterize its microstructure features, the lattice defect evolution, and mechanical properties

In addition to high resolution scanning microscopy and microhardness measurements, positron annihilation spectroscopy (PAS) was used to evaluate the spatial distribution of lattice defects. Our previous investigations proved the feasibility of PAS to determine the lattice defect structure in UFG materials.[12–15]

II. MATERIAL AND EXPERIMENTAL METHODS

Hot-rolled rods of the Ti-6Al-7Nb ELI (IMI 367) alloy for medical application, 20 mm in diameter, manufactured by TIMET were used for the investigation.

MILOŠ JANEČEK, Professor, JOSEF STRÁSKÝ, Ph.D. Student, PETR HARCUBA, Research Fellow, and KRISTÍNA VÁCLAVOVÁ, Undergraduate Student, are with the Department of Physics of Materials, Charles University, Ke Karlovu 5, 12116 Prague 2, Czech Republic. Contact e-mail: janecek@met.mff.cuni.cz JAKUB ČÍŽEK, Professor, is with the Department of Low Temperature Physics, Charles University, Prague, Czech Republic. VERONIKA V. POLYAKOVA, Ph.D. Student, and IRINA P. SEMENOVA, Professor, are with the Ufa State Aviation Technical University, Ufa, Russia.

Manuscript submitted March 1, 2013.

Published online: 30 April 2013

The chemical composition of the alloy was the following: Ti—basic; Al—6.17 pct; Nb—7.05 pct; Fe—0.14 pct; O—0.17 pct; C—0.01 pct; N—0.03 pct; and Ti—balance. The beta-transus temperature according to the material certificate was 1278 K (1005 °C).

Samples in the initial condition were subjected to thermal treatment (TT), including incomplete quenching from 1258 K (985 °C) (20 K below the beta-transus temperature) to room temperature followed by annealing at 973 K (700 °C) for 4 h. The microstructure of the as-received and TT conditions was observed using a light microscope Olympus GX51.

For the HPT process, samples 20 mm in diameter and 2 mm thick were cut from the thermally processed rods by the electrospark method. The sample surface was polished before deformation. During the HPT, the sample was placed between the anvils with a groove of 0.8 mm and pressed under an imposed pressure of 6 GPa. The lower anvil was rotated, and the sample was deformed by shear under the surface friction. The use of the groove excludes sliding of the sample during torsion. Torsion was performed with the rotation speed of 0.5 rpm at room temperature, and a series of specimens after 1/4, 1/2, 1, 3, 5, and 15 rotations were processed.

The high resolution scanning electron microscope FEI Quanta 200 FEG operated at 20 kV was employed for detail investigation of UFG microstructure of the specimens after HPT (10 kV was used to enhance the image contrast in some cases). Back-scattered electron, Z-contrast, and channeling contrast were used for revealing the different microstructural features in the UFG specimens.

An automatic microhardness tester Qness Q10a was used for the evaluation of microhardness variations throughout the surface of specimens after HPT. More than 1000 indents were applied in a square grid with higher density near the specimen center. As a result, more than 100 indents within each ring of 1 mm width were applied.

Lattice defect density variations in individual specimens after HPT were determined by PAS. A Na_2CO_3 positron source with an activity of 1.2 MBq deposited on an approx. 2-μm-thick Mylar foil was used for positron annihilation studies. The source contribution representing a contribution of positrons annihilated in the $^{22}Na_2CO_3$ spot and the covering mylar foil consisted of two weak components with lifetimes of 0.368 and 1.5 ns and relative intensities of 8 pct and 1 pct, respectively. Positron lifetime (LT) measurements were carried out using a high resolution digital spectrometer.[16] The detector part of the digital LT spectrometer consists of two Hamamatsu H3378 photomultipliers coupled with BaF_2 scintillators. Detector pulses are sampled by two ultrafast Acqiris DC211 8 bit digitizers at a sampling frequency of 4 GHz. The digitized pulses are acquired by a PC and analyzed off-line by software using a new algorithm for integral constant fraction timing.[17] The time resolution of the digital LT spectrometer was 145 ps [full width at half maximum (FWHM) of the resolution function for ^{22}Na positron source]. At least 10^7 annihilation events were accumulated in each LT spectrum. Decomposition of LT spectra into exponential components was performed by a maximum likelihood code described in Reference 18.

III. RESULTS

A. *Light Microscopy*

The coarse-grained Ti-6Al-7Nb alloy was received as hot-rolled rods having a duplex structure with grains of the primary α-phase (light area) of an average size of 5.3 μm and a volume fraction of 66 pct distributed in the $\alpha + \beta$ matrix (dark area), see Figure 1.

One of the authors, Polyakova, has shown recently[19] that in order to create the homogeneous UFG structure by the ECAP method, it is effective to enhance the fraction of the thin-plate β-transformed structure, the fragmentation of which occurs easier in the process of SPD. It is also necessary to preserve the fraction of the primary α phase (usually about 20 pct)[20] in the microstructure in order to provide sufficient ductility.[21] In this paper, such a microstructure was obtained by the TT described in the previous section. The structure after TT is characterized by homogeneous distribution of the globular primary α grains in the $\alpha + \beta$ lamellar microstructure—see Figure 2. The volume fraction and the average size of the α phase were 18 pct and 5.3 μm, respectively. The packages of α-phase plates with the average cross size of 330 nm formed in the position of the former martensite occupy about 80 pct of the structure.

B. *SEM Observations*

The microstructure of the as-pressed specimen (*i.e.*, the specimen compressed between the anvils by a pressure of 6 GPa, but without any rotation) and the specimen prepared by HPT (5 revolutions) was observed by SEM using back-scattered electrons.

1. *As-pressed (N = 0) material*

Figure 3 shows the detailed micrograph of the as-pressed material. The contrast of the picture is given by a chemical composition—so-called Z-contrast. Darker

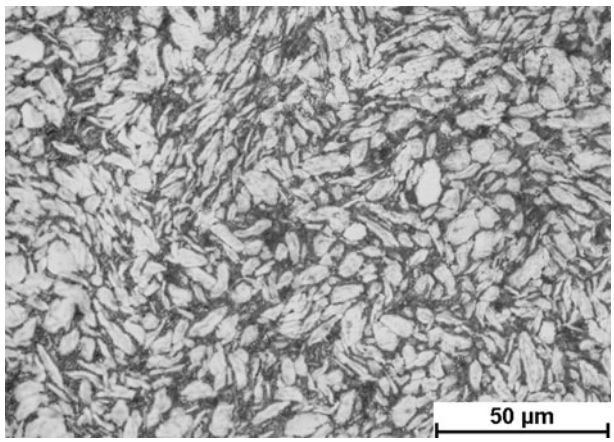

Fig. 1—Light microscopy image of as-rolled Ti-6Al-7Nb cross section.

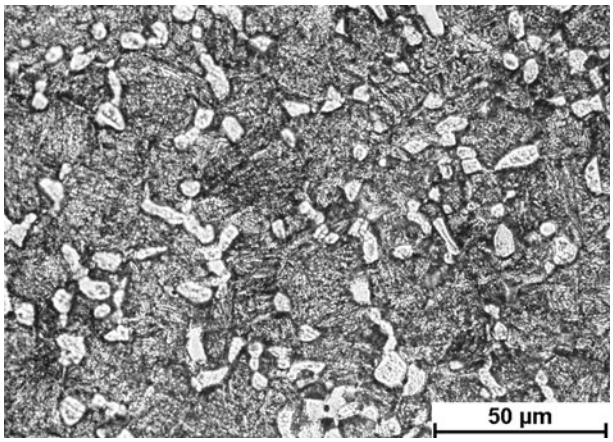

Fig. 2—Light microscopy image of Ti-6Al-7Nb after TT.

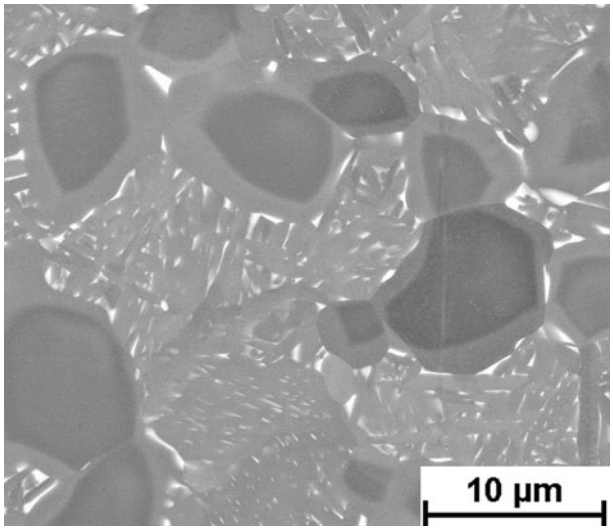

Fig. 3—As-pressed sample ($N = 0$), detail SEM image (back-scattered electrons, Z-contrast).

equiaxed grains are primary alpha grains.[20] Within those grains, two chemically different regions can be distinguished. The interior parts of the grains contain more aluminum and less niobium (see Table I) and therefore appear darker. Diffusion of alpha-stabilizing aluminum and beta-stabilizing niobium must have occurred during thermal processing. The white parts are beta phase particles that are either between primary alpha grains or elongated between alpha lamellae. The resulting microstructure is known as bimodal or duplex. It must be also noted that alpha grains are known to be softer than lamellar areas.[21,22]

Figure 4 is an overview SEM image. Two types of contrast are present: the above-discussed Z-contrast and also the channeling contrast (grains with different orientations may have different contrasts due to different absorption of back-scattered electrons). The white arrows point to the two adjacent alpha grains with different shades, which are caused by their different orientations only. More interestingly, channeling contrast allows the observation

Table I. Chemical Composition of Different Microstructural Features, Measured by EDX

Weight Percent	Average	Alpha—Edge	Alpha—Int.	Beta
Ti	83.0	83.2	85.1	75.7
Al	8.6	8.5	10.0	6.4
Nb	8.5	8.3	4.9	16.4
Fe	0.0	0.0	0.0	1.4

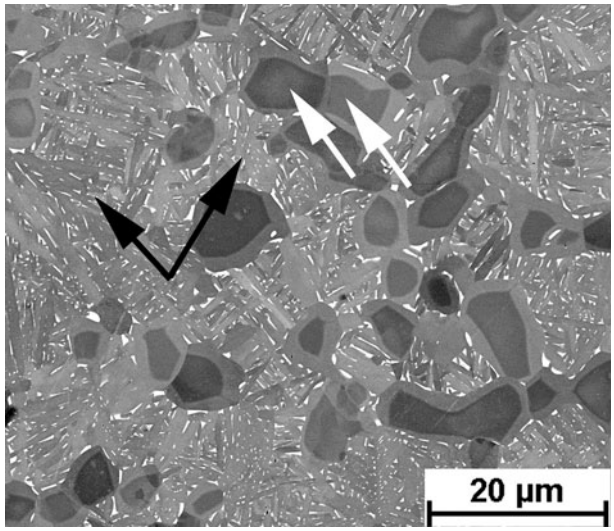

Fig. 4—As-pressed sample ($N = 0$), an overview SEM image. Arrows point to the areas with different channeling contrast.

of different families of parallel lamellae formed in the original beta grain during cooling from the beta region[23] (illustrated by black arrows in two different grains).

The chemical composition was determined by energy dispersive x-ray scattering (EDX). The results are presented in Table I. Note that the results from the EDX may be used only for mutual comparison of different measurements by this method. However, they cannot be quantitatively compared to the results of other methods. Firstly, the average chemical composition was evaluated by x-ray signal acquisition over a sufficiently large area so that the composition is averaged over all microstructural features. The chemical composition slightly differs from the nominal composition of the Ti-6Al-7Nb alloy, proving the qualitative character of these results only. Secondly, the chemical composition was locally measured near the edge and in the interior of alpha grains and in beta particles. The presented results are average values from three different points, but those data should be taken as qualitative only, especially for the beta phase where the beta particle size is comparable to the interaction volume of the electron beam.

2. *Material after HPT ($N = 5$)*

Figure 5 shows the microstructure of the center of the specimen after 5 revolutions. Alpha grains are well distinguishable and their shape is mostly round—similar

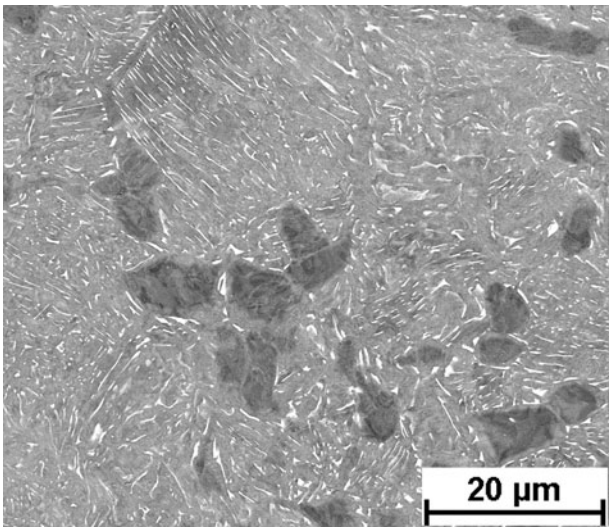

Fig. 5—HPT-deformed material ($N = 5$), center of the sample.

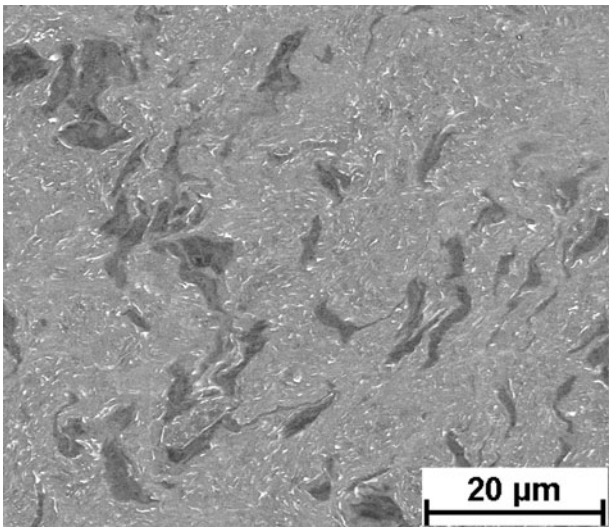

Fig. 6—HPT-deformed material ($N = 5$), 5 mm from the center of the sample.

to the original material. However, each grain is obviously strongly deformed (uneven shade within grain). Alpha + beta phase lamellar areas remain straight in some zones—similar to the as-pressed material—but in other areas, they are already heavily deformed.

Figure 6 shows the typical microstructure of the area that is 5 mm from the center (see scheme in Figure 7). A more deformed microstructure can be observed. Alpha grains are still visible, but their shape is altered due to strong deformation. Each alpha grain is also internally deformed and the whole lamellar part is also deformed.

The microstructure of the zone near the edge of the specimen after 5 revolutions is shown in Figure 8. An even more deformed structure with clear directionality along the direction of deformation (left to right) is seen. However, the original alpha grains are still recognizable.

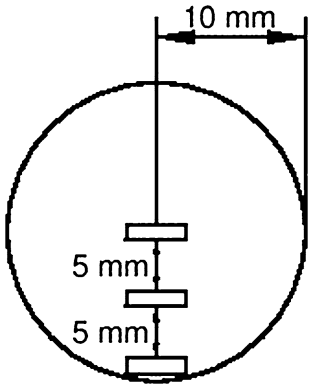

Fig. 7—Scheme of SEM observations.

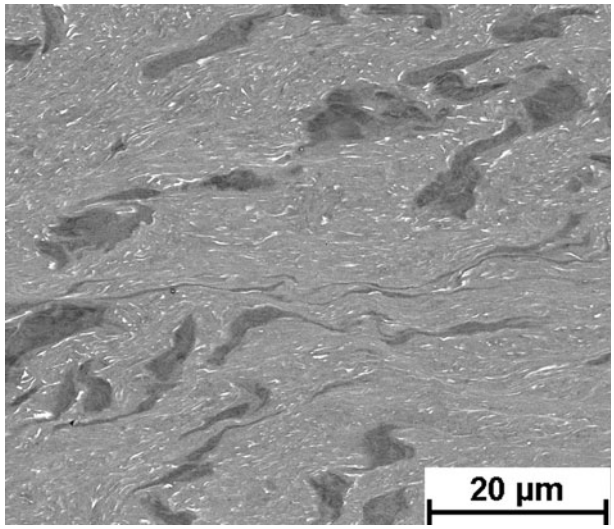

Fig. 8—HPT-deformed material ($N = 5$), edge of the sample.

C. *Microhardness*

Figure 9 shows the microhardness line profiles, *i.e.*, the microhardness variations with the distance from the specimen center toward its edge, in samples subjected to different numbers of HPT revolutions. Each point is an average calculated from more than 100 indents. Error bars show standard deviations. The low precision of measured data is given only by the heterogeneity of the material. Measurement precision is higher by more than one order of the magnitude. Locally heterogeneous microhardness might be associated with heterogenous microstructure; more specifically, the hardness may differ for an indent (with diagonals of approx. 50 μm) in the lamellar area and for another one placed in the alpha grains that are softer.

The results of the measurements indicate that there is a significant increase of microhardness with increasing number of revolutions until $N = 3$. On the other hand, no significant increase of microhardness with distance from the center of the specimen is observed. Some increase is seen only for $N = 1/4$ and $N = 1/2$. For $N = 3$ and higher strains, the microhardness is

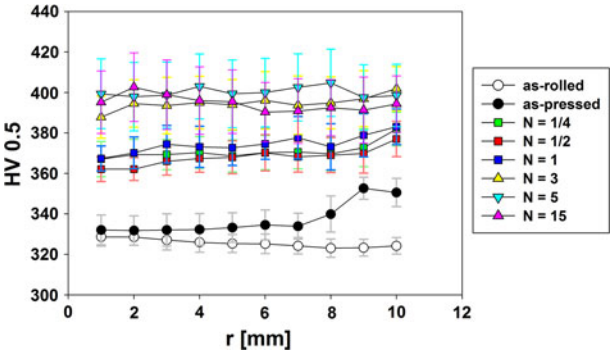

Fig. 9—Dependence of the microhardness on number of HPT turns and the distance from the center of the specimen.

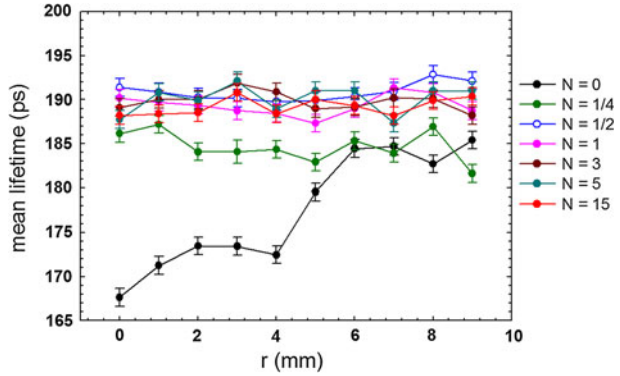

Fig. 10—The mean positron lifetime as a function of the radial distance r from the center of the samples subjected to various number N of HPT revolutions.

homogenous over the whole specimen, which is a favorable result for any potential application, *e.g.*, in microforming technology such as MEMS,[23] microgears,[24] microcups,[25] heat exchangers,[26] *etc*. Finally, an increase in microhardness at the edge of the as-pressed ($N = 0$) specimen is due to material outflow from underneath the pressing anvils, which effectively causes plastic deformation accompanied with microhardness increase. A similar effect was also observed in other materials.[27]

D. *Evolution of Lattice Defects with Strain Due to HPT (Positron Annihilation Spectroscopy)*

Figure 10 shows the dependence of the mean positron lifetime on the radial distance r from the center of the sample subjected to various numbers N of HPT revolutions. In the sample, which was only pressed without any HPT straining ($N = 0$), the mean lifetime at the periphery ($r \geq 6$) is remarkably higher than in the center of the sample, which might be caused by material flowing out of the area of pressing anvils.

HPT straining causes a significant increase of the mean lifetime due to defects introduced by SPD. In the sample subjected to $N = ¼$ HPT revolution, the mean lifetime is increased in the center and becomes approximately constant across the whole sample. Further HPT straining ($N = ½$) leads to an additional increase of the mean lifetime, which finally saturates at the value of ≈190 ps. All samples subjected to more HPT revolutions ($N > ½$) exhibit very similar mean lifetimes. The spatial dependence of the mean lifetime across the sample disk is approximately uniform in all samples subjected to HPT straining ($N \geq ¼$), which proves the formation of a relatively homogeneous structure of defects across the whole sample.

More information can be obtained from the decomposition of positron lifetime spectra into individual components. Figure 11 shows the dependence of the lifetimes of components resolved in positron lifetime spectra on the radial distance r from the center of the sample for materials subjected to various numbers N of HPT rotations. The spatial dependence of relative intensities of these components is plotted in Figure 12.

One can see in Figure 11 that there are three components in the positron lifetime spectra of the samples studied:

(a) A short lived component with lifetime $\tau_1 < 100$ ps and relative intensity I_1 represents a contribution of free positrons annihilated in the delocalized state, *i.e.*, not trapped at defects. This component was found in samples subjected to $N = 0$ and 1/4 HPT revolution only. In samples subjected to more HPT revolutions ($N \geq ½$), the density of defects becomes so high that virtually all positrons are trapped at defects and the free positron component disappeared (saturated positron trapping).[28]
(b) A component with lifetime $\tau_2 \approx 180$ ps and relative intensity I_2. This component which dominates in the positron lifetime spectra of all samples studied can be attributed to positrons trapped at dislocations.
(c) A long-lived component with lifetime $\tau_3 \approx 300$ ps and relative intensity I_3 comes from positrons trapped at larger point defects with open volume corresponding to several vacancies. These defects were likely formed by the agglomeration of deformation-induced vacancies. In order to estimate the size of these vacancy clusters, we performed *ab initio* theoretic calculations of positron parameters for vacancy clusters of various sizes in Ti. Figure 13 shows the calculated dependence of positron lifetime on the size of vacancy clusters consisting of different numbers of vacancies. Obviously, positron lifetime strongly increases with increasing size of vacancy clusters and gradually saturates for large clusters. From the comparison of calculated dependence with experimental lifetimes in Figure 11, one can conclude that the average size of vacancy clusters in HPT-deformed samples corresponds to 4 vacancies.

The as-received material comprises only two components: free positrons with the lifetime $\tau_1 = 84 \pm 3$ ps and the relative intensity $I_1 = 17.6 \pm 0.7$ pct, and positrons trapped at dislocations with the lifetime $\tau_2 = 170 \pm 1$ ps and the relative intensity $I_2 = 82.4 \pm 0.7$ pct. No

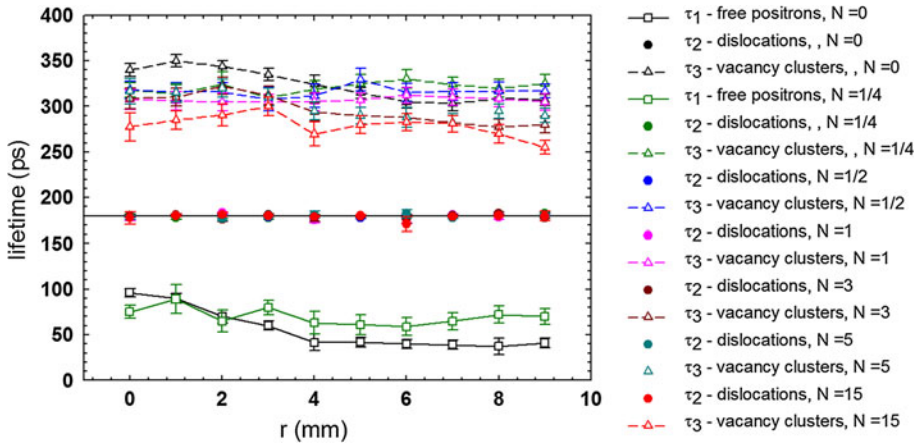

Fig. 11—Dependence of lifetimes of individual positron components on the radial distance r from the center of the sample for materials subjected to various numbers N of HPT rotations.

vacancy clusters were detected in the as-received material.

From the detailed inspection of Figure 12, it becomes clear that in the sample which was only pressed ($N = 0$), the intensity I_1 of the free positron component decreases with increasing distance from the center of the sample, while the intensity I_3 of positrons trapped at vacancy clusters increases. This proves that the concentration of vacancy clusters at the periphery of the sample ($N = 0$) is higher than in the center, most probably due to higher deformation at the periphery where deformed material can flow out of the area of pressing anvils. HPT straining introduces dislocations, which are reflected by an increase of the intensity I_2. One can see in Figure 12 that I_2 increases for the sample subjected to ¼ HPT revolution, and a further increase of I_2 occurs also in the sample strained to ½ HPT revolution. In the latter sample, the density of defects becomes so high that virtually all positrons are trapped and the free positron component cannot be resolved in the spectrum anymore. With increasing torsional strain ($N > ½$), I_2 saturates and remains approximately constant.

Moreover, one can see in Figure 12 that samples subjected to HPT straining ($N \geq ¼$) exhibit approximately uniform spatial dependence of the intensities I_1, I_2, and I_3 across the whole sample disk. This proves that an almost homogeneous structure of defects across the whole sample has already been achieved after ¼ HPT revolution.

Since the samples subjected to HPT straining ($N \geq ¼$) do not exhibit any systematic dependence of positron parameters across the sample except of statistical scattering, the average lifetimes and relative intensities were calculated by averaging of all data measured at each sample. These averaged lifetimes and corresponding relative intensities are plotted in Figure 14 as a function of the number of HPT revolutions. From inspection of the figure, it becomes clear that the density of dislocations strongly increases in the beginning of HPT straining ($N < 1$) and it is accompanied by a disappearance of the free positron component. During further deformation ($N \geq 1$), the dislocation component remains approximately unchanged. The average size of vacancy clusters slightly decreases during HPT straining; see the upper panel in Figure 14.

In the samples $N = 0$ and $N = ¼$ where the free positron component is present in the positron lifetime spectra, one can determine the dislocation density ρ_D by application of the three-state simple trapping model (3-STM)[29]

$$\rho_D = \frac{1}{\nu_D}\frac{I_2}{I_1}\left[\frac{1}{\tau_B} - \frac{1}{\tau_2} + I_3\left(\frac{1}{\tau_2} - \frac{1}{\tau_3}\right)\right], \qquad [1]$$

where $\tau_B = 144$ ps is the bulk positron lifetime in Ti[30] and ν_D is the specific positron trapping rate for dislocations, which is know to fall into the range 10^{-5} to 10^{-4} m^2 s^{-1} for most metals.[31] For the estimation of the dislocation density, we used the average value $\nu_D \approx 0.5 \times 10^{-5}$ m^2 s^{-1}. The dislocation density in the as-received sample is $\rho_D = 1 \times 10^{14}$ m^{-2}. The dislocation density in samples $N = 0$ and $N = ¼$ estimated using the average value $\nu_D \approx 0.5 \times 10^{-5}$ m^2 s^{-1} is plotted in Figure 15 as a function of the radial distance from the center. The dislocation density in both samples slightly increases from the center of the sample toward the edge. The mean dislocation density in the sample subjected to ¼ HPT revolution is 4 times higher than in the as-received material.

The concentration of the vacancy clusters c_{vc} in samples $N = 0$ and ¼ can be estimated within 3-STM from the expression

$$c_{vc} = \frac{1}{n_v \nu_v}\frac{I_3}{I_1}\left[\frac{1}{\tau_B} - \frac{1}{\tau_3} + I_2\left(\frac{1}{\tau_3} - \frac{1}{\tau_2}\right)\right], \qquad [2]$$

where $n_v = 4$ is the average number of vacancies per cluster and $\nu_v \approx 10^{14}$ s^{-1} is the specific positron trapping rate for a vacancy.[31] The concentration of vacancy clusters estimated from Eq. [2] for samples $N = 0$ and ¼ is plotted in Figure 16 as a function of the distance from the center. Obviously, the sample which was only pressed exhibits remarkably higher c_{vc} at the periphery

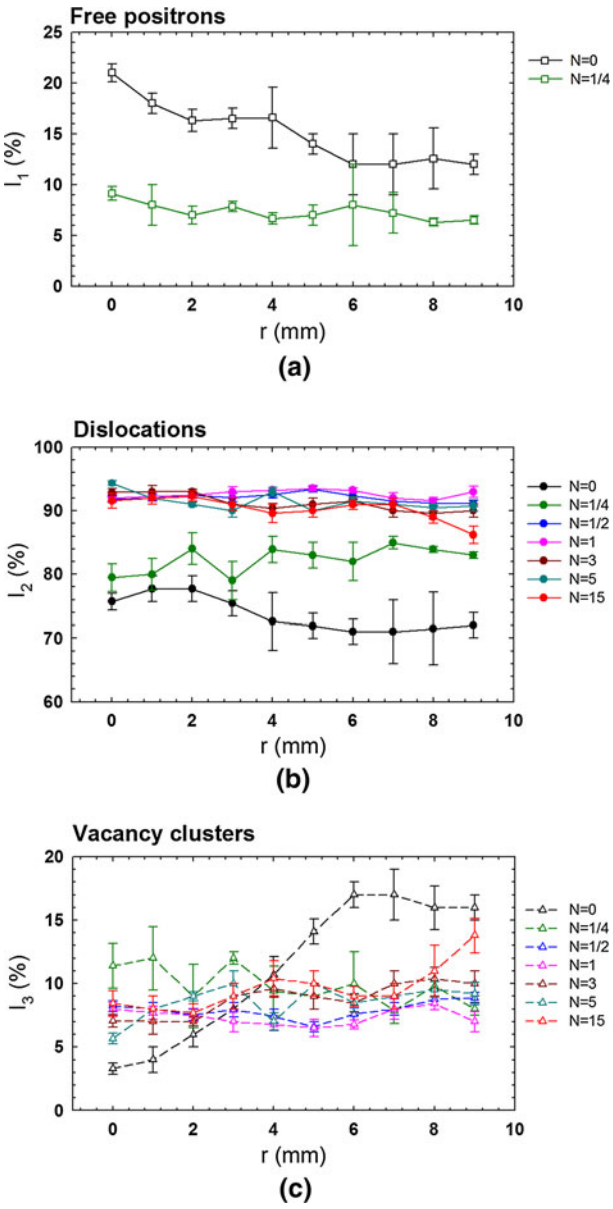

Fig. 12—Relative intensities I_1, I_2, and I_3 for the free positron component (*a*), the contribution of positrons trapped at dislocations (*b*) and vacancy clusters (*c*) for samples subjected to various numbers N of HPT revolutions plotted as a function of the radial distance r from the center of the sample.

compared to the center. On the other hand, the sample subjected to ¼ HPT revolution exhibits a relatively uniform spatial distribution of vacancy clusters. The concentration of vacancy clusters in the sample $N = ¼$ is comparable with that at the periphery of the sample which was only pressed, see Figure 16. An increase of c_{vc} in the center of the sample $N = ¼$ is obviously due to agglomeration of vacancies created by SPD during HPT straining.

In samples subjected to a higher degree of HPT straining ($N \geq ½$), the concentration of defects cannot be determined because of saturated positron trapping which leads to disappearance of the free positron component. Taking into account that the free positron

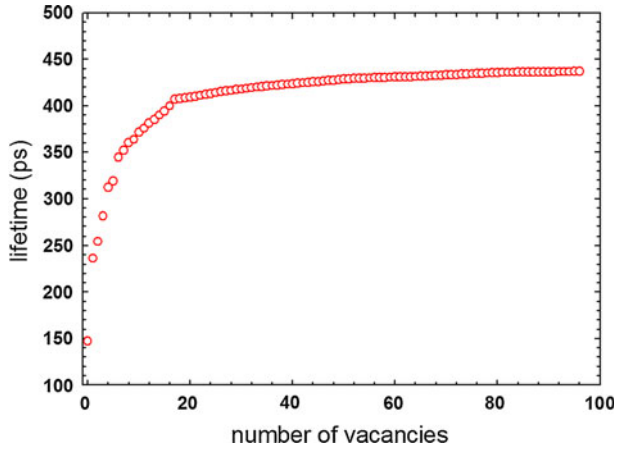

Fig. 13—Calculated positron lifetimes for vacancy clusters in Ti consisting of various numbers of vacancies.

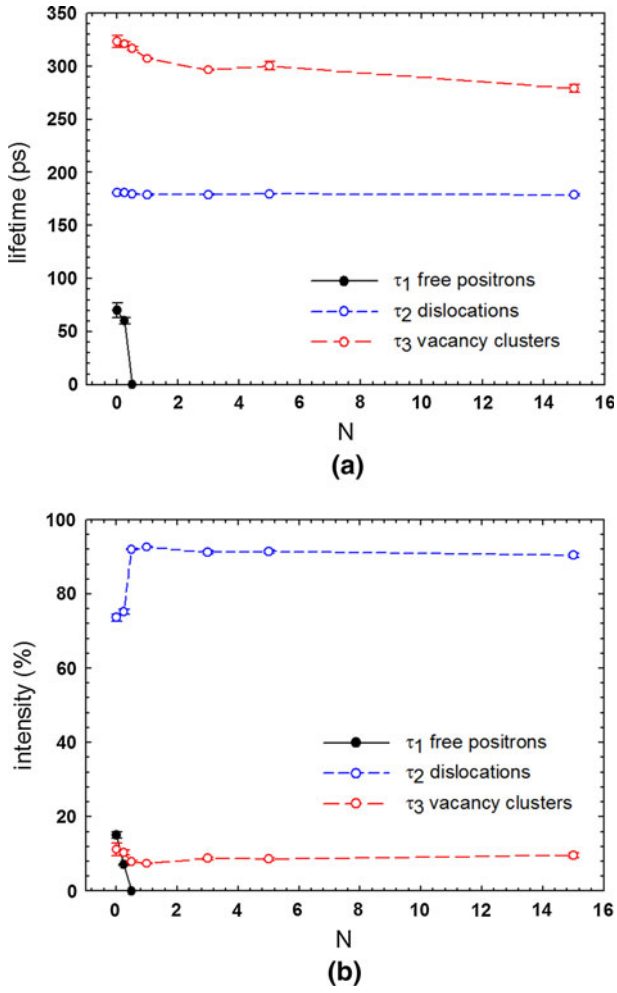

Fig. 14—Positron lifetimes (*a*) and corresponding relative intensities (*b*) averaged over whole sample and plotted as the number of HPT revolutions.

component cannot be resolved when $I_1 < 5$ pct and using the ratio of intensities I_2 and I_3, one can estimate that straining to $N = ½$ leads to an increase of

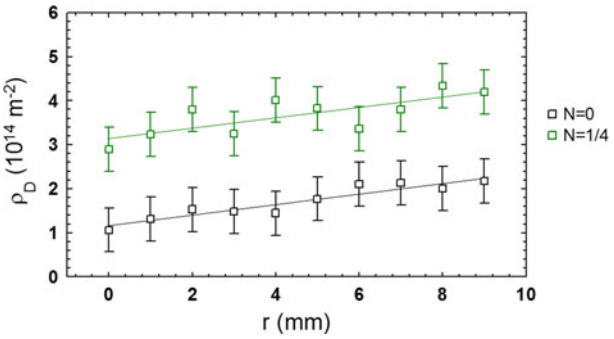

Fig. 15—Dislocation density ρ_D in the sample, which was only pressed ($N = 0$) and the sample subjected to ¼ HPT revolution ($N = ¼$), plotted as a function of the radial distance r from the center.

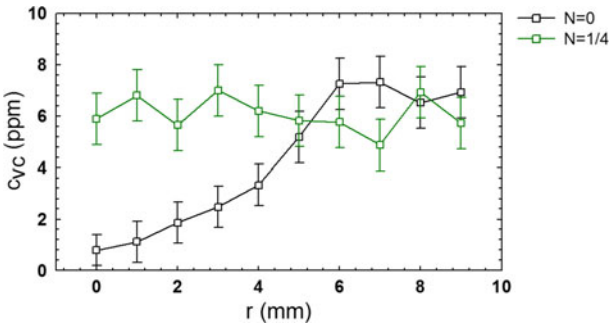

Fig. 16—The concentration c_{vc} of vacancy clusters in the sample which was only pressed ($N = 0$) and the sample subjected to ¼ HPT revolution ($N = ¼$), plotted as a function of the radial distance r from the center.

dislocation density to at least 10^{15} m^{-2} and simultaneously to an increase of c_{vc} to at least 15 ppm. Note that dislocation density might increase during further HPT processing ($N > ½$), but it cannot be detected due to saturated positron trapping. However, if so, then the concentration of vacancy clusters increases in a similar manner and the ratio of concentrations of these two kinds of defects remains unchanged.

IV. DISCUSSION

A. *Effect of Thermal Treatment*

Two-step TT results in a typical duplex microstructure consisting of round primary alpha grains and lamellar $\alpha + \beta$ structure. Chemical analysis proved that the interiors of the primary alpha grains are aluminum enriched and niobium depleted, whereas the rim of those grains has the average composition. We assume that the interior of the primary alpha grains having the volume fraction of approximately 10 pct are original alpha grains of the as-received (as-rolled) material that remain in the material during annealing at 1258 K (985 °C). These alpha grains started to grow during annealing at 973 K (700 °C), but the temperature is not sufficiently high to cause the diffusional change in the composition of the primary alpha grains in favor of α-stabilizing elements. As a result, the interiors of the primary alpha grains have different chemical compositions than their rims.

Contrarily, beta particles are aluminum depleted and strongly niobium enriched. Beta particles also include detectable iron content. Iron is the typical impurity in Ti alloys and even in a low content (<1 wt pct), it helps to stabilize the beta phase.[32]

B. *Relation Between Defect Structure, Microstructure, and Microhardness*

SEM observations confirm that after HPT deformation, primary alpha grains and $\alpha + \beta$ lamellaes are present in the microstructure. However, microhardness measurements and PAS cannot distinguish between those microstructural features. The approximate size of an indent is 50 μm and therefore it is too large to distinguish between these two regions. On the other hand, each indentation does not represent the measurement of a truly average material. The results of microhardness are therefore heterogeneous. Interestingly, the heterogeneity (represented as standard deviation from the mean value) increases with increasing strain. This suggests that the difference between hardness of the alpha grains and $\alpha + \beta$ lamellar structure increases with increasing strain. Most probably, $\alpha + \beta$ lamellar structure is significantly hardened. The final answer to this assumption may be provided by more detailed microhardness or nanohardness measurements.

For the as-pressed sample ($N = 0$), the outflow of the material between the anvils is captured by significant increase in vacancy clusters in the periphery region, but no increase in dislocation density occurs. Microhardness increases significantly, proving the important effect of vacancy hardening.[33]

The defect structure is already homogenous from $N = 1/2$ HPT revolution, while the microhardness is homogenous from $N = 3$ HPT revolutions only. On the other hand, the microstructure is not entirely homogenous even after $N = 5$ HPT revolutions. The evolution of primary alpha grains as observed by SEM is rather independent of the evolution of point and line defects as evaluated by PAS. Several mechanisms like vacancy hardening, dislocation density, and microstructure refinement are responsible for the significant hardness increase which is not directly related to a single characteristic quantity.

V. CONCLUSIONS

The following conclusions can be drawn from the presented investigations of the ultrafine-grained Ti-6Al-7Nb biocompatible alloy prepared by HPT up to 15 revolutions:

1. Thermal treatment before HPT resulted in duplex microstructure with chemically heterogeneous primary alpha grains having 18 pct volume fraction. Primary alpha grains provide sufficient ductility for SPD, whereas the major $\alpha + \beta$ lamellar microstructure becomes more easily fragmented and hardened.

2. SEM observations revealed heavily deformed primary alpha grains surrounded by significantly fragmented $\alpha + \beta$ microstructure after 5 HPT revolutions.
3. Microhardness significantly increases (from 330 to 400 HV 0.5) with increasing strain, but it is heterogenous due to heterogenous microstructure. Heterogeneity of microhardness increases with increasing strain, suggesting that the $\alpha + \beta$ lamellar microstructure is more hardened than primary alpha grains.
4. Positron annihilation spectroscopy showed significant increase of dislocation density (approx. 10^{15} m^{-2}) and of the concentration of vacancy clusters (15 ppm) after ½ of the HPT revolution.
5. The defect structure is already homogenous after ½ HPT revolution, while the microhardness becomes homogenous after three HPT revolutions.

ACKNOWLEDGMENTS

This work was financially supported by the Czech Ministry of Education and Youth under the grant LH12217. Partial financial support by the Czech Science Foundation under the project P107/12/1025 is also acknowledged. One of the authors J.C. acknowledges financial support from the Czech Science Foundation (project P108/12/G043).

REFERENCES

1. M. Geetha, A.K. Singh, R. Asokamani, and A.K. Gogia: *Prog. Mater. Sci.*, 2009, vol. 54, pp. 397–425.
2. C. Leyens and M. Peters: *Titanium and Titanium Alloys*, Wiley-VCH Verlag, 2003, pp. 423–51.
3. K.S. Katti: *Colloids Surf. B*, 2004, vol. 39, pp. 133–42.
4. M. Niinomi: *J. Mech. Behav. Biomed. Mater.*, 2008, vol. 1, pp. 30–42.
5. R.Z. Valiev and T.G. Langdon: *Prog. Mater. Sci.*, 2006, vol. 51, pp. 881–981.
6. A.P. Zhilyaev and T.G. Langdon: *Prog. Mater. Sci.*, 2008, vol. 53, pp. 893–979.
7. H.S. Kim: *J. Mater. Proc. Technol.*, 2001, vol. 113, pp. 622–26.
8. Y. Saito, H. Utsunomiya, N. Tsuji, and T. Sakai: *Acta Mater.*, 1999, vol. 47, pp. 579–83.
9. V.N. Varyutkhin, Y. Beygelzimer, S. Synkov, and D. Orlov: *Mater. Sci. Forum*, 2006, vols. 503–504, pp. 335–38.
10. X. Yang, Y. Okabe, H. Miura, and T. Sakai: *J. Mater. Sci.*, 2012, vol. 47, pp. 2823–30.
11. Z. Horita, D.J. Smith, M. Furukawa, M. Nemoto, R.Z. Valiev, and T.G. Langdon: *J. Mater. Res.*, 1996, vol. 11, pp. 1880–90.
12. R. Kužel, Z. Matěj, V. Cherkaska, J. Pešička, J. Čížek, I. Procházka, and R.K. Islamgaliev: *J. Alloys Compd.*, 2004, vol. 378, pp. 242–47.
13. M. Janeček, J. Čížek, M. Dopita, R. Král, and O. Srba: *Mater. Sci. Forum*, 2008, vols. 584–586, pp. 400–45.
14. Z. Matěj, R. Kužel, M. Dopita, M. Janeček, J. Čížek, and T. Brunátová: *Int. J. Mater. Res.*, 2009, vol. 100, pp. 880–83.
15. R. Kužel, M. Janeček, Z. Matěj, J. Čížek, M. Dopita, and O. Srba: *Metall. Mater. Trans. A*, 2010, vol. 41A, pp. 1174–90.
16. F. Bečvář, J. Čížek, I. Procházka, and J. Janotová: *Nucl. Instrum. Methods A*, 2005, vol. 539, pp. 372–85.
17. F. Bečvář: *Nucl. Instrum. Methods B*, 2007, vol. 261, pp. 871–74.
18. I. Procházka, I. Novotný, and F. Bečvář: *Mater. Sci. Forum*, 1997, vols. 255–257, pp. 772–74.
19. V.V. Polyakova and I.P. Semenova: *Modern Problems of Science and Education*, 2012, vol. 6, in Russian.
20. J. Mueller, H.J. Rack, and L. Wagner: Ti-2007, *Science and Technology*, M. Niinomi, S. Akiyama, M. Hagiwara, M. Ikeda, and K. Maryama, eds., JIMIC 5, 2007, pp. 383–87.
21. R. Boyer, G. Welsh, and E. Collings: *Material Properties Handbook—Titanium Alloys*, ASM International, Materials Park, OH, 1994.
22. N. Poondla, T.S. Srivatsan, A. Patnaik, and M. Petraroli: *J Alloys Compd.*, 2009, vol. 486, pp. 162–67.
23. Y. Estrin, M. Janeček, G.I. Raab, R.Z. Valiev, and A. Zi: *Metall. Mater. Trans. A*, 2007, vol. 38A, pp. 1906–09.
24. W.J. Kim and Y.K. Sa: *Scripta Mater.*, 2006, vol. 54, pp. 1391–95.
25. X. Ma, R. Lapovok, C. Gu, A. Molotnikov, Y. Estrin, E.V. Pereloma, C.H.J. Davies, and P.D. Hodgson: *J. Mater. Sci.*, 2009, vol. 44, pp. 3807–12.
26. X.G. Qiao, N. Gao, Z. Moktadir, M. Kraft, and M.J. Starink: *J. Micromech. Microeng.*, 2010, vol. 20, p. 045029.
27. J. Vrátná, M. Janeček, J. Čížek, D.J. Lee, E.Y. Yoon, and H.S. Kim: *J. Mater. Sci.*, 2013, DOI:10.1007/s10853-013-7151-x.
28. J. Čížek, M. Janeček, O. Srba, R. Kužel, Z. Barnovská, I. Procházka, and S. Dobatkin: *Acta Mater.*, 2011, vol. 59, pp. 2322–29.
29. R. West: Positrons in Solids, *Topics in Current Physics*, P. Hautojärvi, ed., Springer, Berlin, 1979, pp. 89–115.
30. J.M. Campillo Robles, E. Ogando, and F. Plazaola: *J. Phys. Condens. Matter*, 2007, vol. 19, p. 176222.
31. P. Hautojärvi and C. Corbel: *Proceedings of the International School of Physics "Enrico Fermi", Course CXXV*, A. Dupasquier and A.P. Mills, eds., IOS Press, Varena, 1995, pp. 491–506.
32. M. Mhaede, L. Wagner, and K. Ibrahim: *Int. J. Mater. Res.*, 2013. doi:10.3139/146.110920.
33. M. Zehetbauer: *Key Eng. Mater.*, 1995, vols. 97–98, pp. 287–306.